complex with S2 in the presence of polyP (Fig. 4B), suggesting that binding of S2 to polyP helped in the formation of a complex with Lon. Addition of polyP (without substrates) did not stimulate the adenosine triphosphatase activity of Lon. Thus, the stimulation of S2 degradation can be ascribed mainly to the formation of a complex between Lon and S2 in the presence of polyP.

Escherichia coli contains substantial amounts of ribosomal proteins, including S2, as disassembled (free) forms during exponential growth on a rich medium, but little on a minimal medium (*16*). About 17% of total S2 protein exists as the free form (*16*), and such ribosomal proteins may be subjected to Lon-dependent degradation (*17*). Thus, it is likely that the S2 protein found in fraction P9 was free from ribosomes, and that polyP was involved in the degradation of free ribosomal proteins after the downshift. Degradation of ribosomal proteins should release amino acids for synthesis of the key enzymes required for adaptations to starvation, as well as reduce translational activity during starvation. Most substrates for polyP-dependent degradation were basic ribosomal proteins that could bind to polyP [see supplementary material (*18*)]. In assays of polyP binding to proteins in *E. coli* lysates, most proteins were contained within the ribosome fractions, but also included Lon as well as ribosome-associated proteins. Thus, it is likely that the ribosomal proteins are the major substrates (in terms of mass) for this system. When we used intact ribosomes as substrates for Lon, Lon with polyP was ineffective in degrading intact ribosomes, but did act on ribosomes treated with ribonuclease (RNase) (*18*). Thus, polyP alone did not disassemble the ribosome, but polyP and Lon together degraded free ribosomal proteins, as well as those in the RNase-distorted ribosome. Our findings may provide insights into the regulation of protein degradation when cells are stressed or enter the stationary phase.

References and Notes

1. A. Kornberg, *J. Bacteriol.* **177**, 491 (1995).
2. A. Kuroda, H. Murphy, M. Cashel, A. Kornberg, *J. Biol. Chem.* **272**, 21240 (1997).
3. D. Ault-Riché, C. D. Fraley, C.-M. Tzeng, A. Kornberg, *J. Bacteriol.* **180**, 1841 (1998).
4. A. Kuroda *et al.*, *Proc. Natl. Acad. Sci. U.S.A.* **96**, 14264 (1999).
5. C. G. Miller, in Escherichia coli *and* Salmonella*: Cellular and Molecular Biology*, F. C. Neidhardt *et al.*, Eds. (American Society for Microbiology, Washington, DC, ed. 2, 1996), pp. 938–954.
6. N. Mizushima *et al.*, *Nature* **395**, 395 (1998).
7. M. R. Maurizi, *Experientia* **48**, 178 (1992).
8. C. H. Chung, A. L. Goldberg, *Proc. Natl. Acad. Sci. U.S.A.* **79**, 795 (1982).
9. A.L. Goldberg, *Eur. J. Biochem.* **203**, 9 (1992).
10. S. Mizusawa, S. Gottesman, *Proc. Natl. Acad. Sci. U.S.A.* **80**, 358 (1983).
11. Lon protease fused with maltose-binding protein (MBP-Lon) was purified from *E. coli* (pMAL-Lon) as described (*19*).
12. NH_2-terminal sequences of the proteins tested were ATVSMRDMLKAGVHF, MQVILLDKVAN, and MKTFTAKPETV, which matched precisely the amino acid sequences of S2 (residues 2 to 16), L9 (residues 1 to 11), and L13 (residues 1 to 11), respectively.
13. A *rpsB* (S2) gene was amplified by polymerase chain reaction with primers 5′-ATGGCAACTGTTTCCATGCGCG-3′ and 5′-CTCAGCTTCTACGAAGCTTTCT-3′, and then inserted into pBAD-TOPO plasmid (Invitrogen) to construct a S2–V5-epitope fusion gene. S2–V5-epitope fusion protein was expressed only in the presence of 0.2% L-arabinose.
14. B. T. Wimberly *et al.*, *Nature* **407**, 327 (2000).
15. Y. Ishii *et al.*, *J. Biochem.* **127**, 837 (2000).
16. B. Ulbrich, K. H. Nierhaus, *Eur. J. Biochem.* **57**, 49 (1975).
17. K. Nishi, J. Schnier, *Mol. Gen. Genet.* **212**, 177 (1988).
18. Supplementary Web material is available on *Science* Online at www.sciencemag.org/cgi/content/full/293/5530/705/DC1.
19. S. Sonezaki *et al.*, *Appl. Microbiol. Biotechnol.* **42**, 313 (1994).
20. M. Kanemori, H. Yanagi, T. Yura, *J. Bacteriol.* **181**, 3674 (1999).
21. Purified protein was diluted at various concentrations of ^{32}P-$polyP_{700}$ (295 cpm/pmol) in 50 μl of 20 mM tris-HCl buffer (pH 7.4) and 5 mM $MgCl_2$. After incubation at 37°C for 5 min, the mixture was transferred to a nitrocellulose filter (0.45 μm), and then free ^{32}P-polyP was washed off with the same buffer containing 100 mM NaCl. The radioactivity remaining on the filter, corresponding to the amount of polyP-protein complex, was measured by scintillation counting.
22. *E. coli* MG1655 (in late exponential phase) was subjected to lysis with lysozyme and centrifuged (30 min, 30,000*g*) and then the supernatant was applied onto a phospho-cellulose column (P11, Whatman) equilibrated with 0.1 M potassium P_i. Fractions were eluted with a linear gradient of 0.1 to 0.4 M potassium P_i. Fraction P9 eluted near 0.4 M potassium P_i.
23. C. Cachia, P.-J. Flamion, J.-P. Schreiber, *J. Chromatography* **539**, 343 (1991).
24. Fraction P9 (*22*) containing the S2 protein was applied onto a MiniQ column (Smart, Amersham-Pharmacia-Biotech) equilibrated with 20 mM tris-HCl (pH 7.4), 0.5 mM dithiothreitol, and 1 mM EDTA. The S2 protein was eluted with a linear gradient from 20 to 500 mM NaCl. The S2 protein was also purified from 70*S* ribosome as described (*23*).

25. We thank T. Yura and M. Kanemori for providing the protease mutants. Some of the protease mutants are originally from S. Gottesman (NIH). We thank Y. Ishii for providing plasmid pMAL-Lon, and I. R. Lehman, D. Kaiser, N. Rao, C. D. Fraley, L. Bertsch, and K. Mizuta for helpful suggestions. Supported by grants from the Ministry of Education, Science and Culture of Japan and the National Institutes of Health.

4 April 2001; accepted 25 May 2001

The Crystal Structure of Uncomplexed Actin in the ADP State

Ludovic R. Otterbein, Philip Graceffa, Roberto Dominguez*

The dynamics and polarity of actin filaments are controlled by a conformational change coupled to the hydrolysis of adenosine 5′-triphosphate (ATP) by a mechanism that remains to be elucidated. Actin modified to block polymerization was crystallized in the adenosine 5′-diphosphate (ADP) state, and the structure was solved to 1.54 angstrom resolution. Compared with previous ATP-actin structures from complexes with deoxyribonuclease I, profilin, and gelsolin, monomeric ADP-actin is characterized by a marked conformational change in subdomain 2. The successful crystallization of monomeric actin opens the way to future structure determinations of actin complexes with actin-binding proteins such as myosin.

Actin is the major component of the thin filaments of muscle cells and of the cytoskeletal system of nonmuscle cells, taking part in a multitude of biological functions (*1*, *2*). Monomeric actin (G-actin) assembles under physiological salt concentrations to form polymers (F-actin), a property that has so far prevented crystallization of the uncomplexed monomer. Structures have been determined, however, for complexes of actin with deoxyribonuclease I (DNase I) (*3*), gelsolin (*4*, *5*), and profilin (*6*), all proteins that prevent polymerization.

Actin and most members of its structural class, which includes the hsp70 molecular chaperones, hexokinase, and the sugar kinases (*7*, *8*), appear to undergo a conformational change coupled to ATP hydrolysis. In actin, this conformational change may play a critical role in filament dynamics (*1*, *9*). ADP-actin filaments exhibit a higher susceptibility to depolymerizing proteins (*2*). The addition of inorganic phosphate (P_i) or P_i analogs helps stabilize the ADP-actin filaments (*10*, *11*), presumably by mimicking an ADP·P_i state. The different properties of ADP·P_i- and ADP-actin filaments have been correlated with differences in their tertiary structures (*12*, *13*). Actin subdomain 2 and, in particular, its DNase I binding loop, which is involved in intermonomer interactions within the filament (*14*), have been directly linked with the conformational change by studies with electron microscopy (*12*, *15*), proteolysis (*16–18*), and fluorescence spectroscopy (*19–21*).

Boston Biomedical Research Institute, 64 Grove Street, Watertown, MA 02472, USA.

*To whom correspondence should be addressed. E-mail: dominguez@bbri.org

Crystal structures of ATP- and ADP-bound actin complexed with DNase I are very similar (*3*). However, the ADP structure was obtained after hydrolysis of ATP within the crystals that were initially grown in the ATP state (*3*). It is therefore possible that this structure was constrained in the ATP state by crystal contacts or by interactions between DNase I and actin subdomain 2 (*8*). Here we present direct, high-resolution, crystallographic evidence for a conformational change in monomeric actin subdomain 2 upon P_i release.

To crystallize actin, we found that its ability to polymerize was blocked by covalent binding of the fluorescent probe tetramethylrhodamine-5-maleimide (TMR) to Cys^{374} (*22*). The modified actin can be crystallized in the absence of other proteins with ADP bound to the active site (*23*). The crystals, which diffract x-rays to at least 1.4 Å resolution, grow as plates (~0.05 mm by 0.1 mm by 0.4 mm) with a characteristic red color due to the presence of the probe.

The structure was solved by molecular replacement and refined to 1.54 Å resolution (*23*). Overall, the ADP structure is similar to previous ATP-actin structures (Fig. 1). However, differences occur in the orientation of subdomains 2 and 4, which, compared to the ATP structures, are rotated by ~10° and ~5°, respectively (Fig. 2). In addition, the DNase I binding loop within subdomain 2 (residues His^{40}-Gly^{48}) is folded as an α helix, whereas in previous actin structures it is either disordered or folded as a β turn (Fig. 2). Minor differences also occur at the opposite side of the molecule, in subdomain 1, where TMR binds in a hydrophobic pocket near the COOH-terminus (Fig. 1).

Just as observed in myosin, where a minor change near the nucleotide γ-phosphate becomes gradually amplified into a large movement of its light-chain binding domain (*24*), a relatively small alteration in the nucleotide-binding site of actin translates into a significant conformational change in subdomain 2. In the ATP-actin structures the nucleotide β- and γ-phosphates are sandwiched between two structurally equivalent β-hairpins (Asp^{11}-Lys^{18} and Asp^{154}-His^{161}), belonging to the two homologous actin subdomains 1 and 3. These β-hairpins, thought to play a critical role in ATP hydrolysis (*7*, *8*), are related by a pseudo–twofold rotation centered halfway between the β- and γ-phosphates and exhibit closely related sequences (Fig. 3). The catalytic Ca^{2+} lies below the nucleotide on the pseudo–twofold axis and is coordinated, in the ATP structures, by four water molecules and two O atoms from the β- and γ-phosphates in a tetragonal bipyramidal arrangement. (This description is based on the structure of the yeast actin-gelsolin complex which, at 1.9 Å, is the highest resolution structure of actin in the ATP state so far available; Protein Data Bank code 1YAG). In the ADP structure, the positions of the nucleotide and Ca^{2+} remain virtually unchanged (Figs. 2 and 3). Also conserved in both nucleotide states is a strong bidentate interaction between the NZ atom of Lys^{18} with two O atoms from the α- and β-phosphates. Differences occur in the coordination of the Ca^{2+}, however, which in the ADP structure interacts with six water molecules and a single O atom from the nucleotide β-phosphate, in a nearly ideal pentagonal bipyramidal arrangement (Fig. 3). The water molecules that coordinate the Ca^{2+} are held in place through interactions with the side chains of Asp^{11}, Asp^{154}, and Gln^{137}.

Central to the structural transition caused by release of the γ-phosphate is Ser^{14} at the top of the β-hairpins from subdomain 1. In the ADP structure, the side chain of Ser^{14} adopts a different rotamer so that its Oγ, which in the ATP structures is hydrogen-bonded to an O atom from the γ-phosphate, is now in contact with an O atom from the β-phosphate. This allows the polypeptide backbone around Ser^{14} to move toward the nucleotide by ~1.0 Å, sufficient to further disrupt the hydrogen-bonding network with its neighbors, Ser^{33} and Tyr^{69}, which are the two amino acids that mark the beginning and end of subdomain 2 (Figs. 2 and 3).

In both the ADP and ATP structures the Oγ of Ser^{33} is hydrogen-bonded to the main-

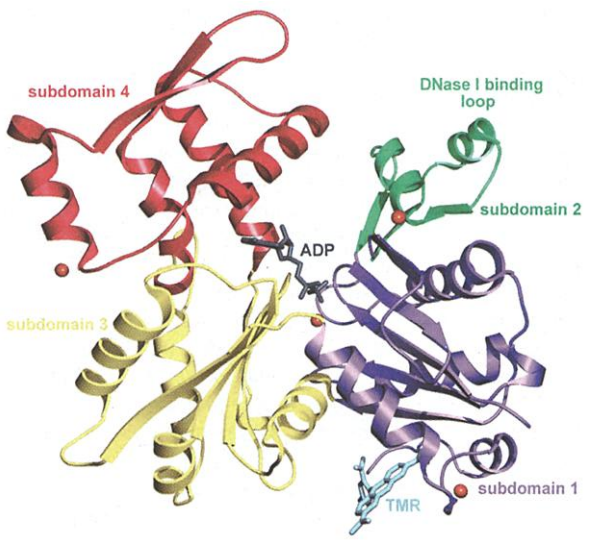

Fig. 1. Ribbon representation of the structure of uncomplexed actin in the ADP state. The four subdomains of actin are represented in different colors: subdomains 1 (purple), 2 (green), 3 (yellow), and 4 (red). The DNase I binding loop, which is folded as an α helix in this structure, is located toward the upper part of subdomain 2 (see also Fig. 2). ADP is bound at the center of the molecule, where the four actin subdomains meet. As suggested by the conformational differences observed between our ADP-actin structure and previous ATP-actin structures, nucleotide-dependent differences in this location may provide a mechanism to change the orientations of the actin subdomains relative to each other. Four Ca^{2+} ions bound to the actin monomer in the crystals are represented as gold-colored spheres. One of the Ca^{2+} ions, termed primary or catalytic, is bound in close association with the nucleotide. The other three Ca^{2+} ions are bound to subdomains 1, 2, and 4 on the surface of the molecule and may correspond to secondary cation-binding sites of actin (*25*). Tetramethylrhodamine-5-maleimide (TMR), which is covalently attached to Cys^{374}, binds in a hydrophobic pocket near the COOH-terminus in actin subdomain 1.

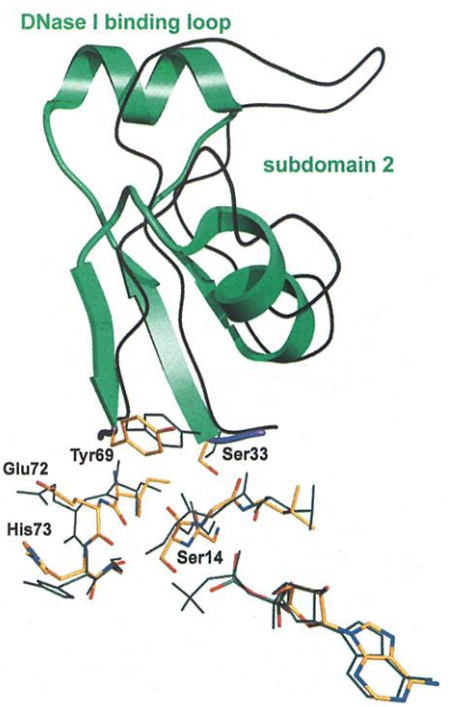

Fig. 2. Actin subdomain 2. This view of subdomain 2 is from the active site and is perpendicular to that shown in Fig. 1. The new ADP-actin structure is represented in green. Some important amino acids in the active site are shown with an atom-type color-coding scheme. For comparison, the ATP-actin structure from the DNase I complex is also shown (black trace). The plot was generated after best fitting actin subdomains 1 and 3, whose orientations remain largely unchanged in all the actin structures (independent of nucleotide state). In the ADP-actin structure, subdomain 2 is rotated by ~10° compared with any of the ATP-actin structures (*3*–*6*). The general orientation of subdomain 2 is similar among all the ATP-actin structures, but the conformation of the DNase I binding loop, which in our ADP-actin structure is folded as an α helix, is either a β turn [DNase I and profiling complexes (*3*, *6*)] or a disordered loop [gelsolin complexes (*4*, *5*)].

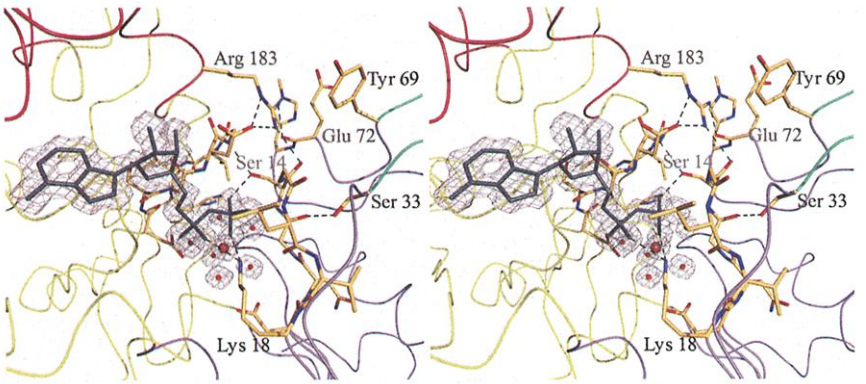

Fig. 3. Close-up stereo view of the nucleotide-binding site in the ADP state. The different ribbon colors (color-coded as in Fig. 1) represent the four actin subdomains that converge around the nucleotide. Represented by dashed lines are some of the most important hydrogen-bonding contacts involving Ser^{14}, Lys^{18}, Ser^{33}, and Arg^{183} (see main text). The $2F_o - F_c$ electron density map around the ADP, Ca^{2+}, and the six water molecules that help coordinate the Ca^{2+} is shown contoured at 1.4σ. The Ca^{2+} and the nucleotide β-phosphate are sandwiched in between two structurally equivalent β-hairpins belonging to actin subdomains 1 and 3. These β-hairpins are related by a pseudo twofold rotation and display homologous sequences: Asp^{11}-Asn-Gly-Ser-Gly-Leu-Val-Lys^{18} and Asp^{154}-Ser-Gly-Asp-Gly-Val-Thr-His^{161} (all atoms are shown in the figure). The two amino acids that mark the beginning and end of subdomain 2 (green ribbon)—Ser^{33} and Tyr^{69}—as well as Glu^{72}, whose peptide bond is flipped around in the ADP structure, are also shown.

Table 1. Summary of data collection and refinement statistics.

Parameter	Value
Data collection	
Space group	*C2*
Unit cell parameters	
a, *b*, *c* (Å)	112.8, 37.5, 85.3
α, β, γ (°)	90.0, 108.3, 90.0
Resolution range (Å)	82.0–1.54
No. of unique reflections	48,138
Completeness (%)	97.0
Redundancy	7.6
R_{merge} (%)*	6.1
Refinement and model quality	
Resolution (Å)	20.0–1.54
σ-cutoff	None
R_{factor} (%; all reflections)†	17.9
Free R_{factor} (%)‡	22.3
Ramachandran	
Most favored (%)	92.8
Additionally allowed (%)	7.2
Generously allowed (%)	0.0
Disallowed (%)	0.0
rmsd in bond distance (Å)	0.012
rmsd in bond angle (°)	2.4
rmsd in dihedral angle (°)	25.0
rmsd in improper angle (°)	2.08
Average *B* factor (protein, waters; Å²)	18.3, 34.8

*$R_{merge} = \Sigma|I - \langle I\rangle|/\Sigma I$, where I is the observed intensity of an individual reflection, and $\langle I\rangle$ is the mean intensity of that reflection. †$R_{factor} = \Sigma||F_o| - |F_c||/\Sigma|F_o|$, where F_o and F_c are observed and calculated structure factors, respectively. ‡Free R_{factor} same as R_{factor}, but calculated for a subset of the reflections (5%), which were omitted during the refinement and used to monitor its convergence. rmsd, root mean square deviation.

chain carbonyl of Gly^{13} from the β-hairpin in subdomain 1. Thus, the movement of the β-hairpin in going from the ATP to the ADP structure is mirrored by Ser^{33}, which undergoes a rotamer change and main-chain backbone shift of ~1.5 Å (Fig. 2). A loop (Pro^{70}-Thr^{77}), containing the constitutively methylated His^{73}, connects the COOH-terminal end of subdomain 2 to an α helix in subdomain 1. Because this loop lies adjacent to Ser^{14} in the ADP and ATP structures, it also undergoes major reorganization. The peptide bond between Glu^{72} and His^{73} flips around and the backbone at Glu^{72} moves ~2.0 Å toward the nucleotide site in the ADP structure. The net result from the combined changes at both ends of subdomain 2 is a ~10° rigid body rotation of the entire subdomain (Fig. 2).

Besides affecting the orientation of subdomain 2, the reorganization of the His^{73}-loop in the ADP structure also allows for a new hydrogen-bonding contact between the main-chain carbonyl of Glu^{72} and the side-chain NH_2 of Arg^{183} (Fig. 3). Arg^{183} belongs to actin subdomain 4, and in both the ATP and the ADP structures it is involved in two additional interactions. These are a hydrogen-bonding contact with the main-chain carbonyl of Ser^{14} and a salt bridge with the side chain of Asp^{157} (Fig. 3). Ser^{14} and Asp^{157} occupy equivalent positions with respect to the pseudo twofold rotation that relates actin subdomains 1 and 3. Arg^{183} provides the most obvious communication route between the ATP site, the His^{73}-loop, and subdomain 4, thereby playing a key role in fine-tuning the orientation of subdomain 4, which is rotated by ~5° compared with the ATP structures. Because subdomain 4 is at small radius within the filament (*14*), even minor changes in this domain may have major effects on the structure and stability of the polymer.

Differences between the ADP- and previous ATP-actin structures also occur in the DNase I binding loop (residues His^{40} to Gly^{48}) within subdomain 2 (Fig. 2). Whereas in the ADP structure the loop is folded as an α helix, in the two actin-gelsolin complexes (*4*, *5*) it is disordered and cannot be visualized, and in the actin-profilin (*6*) and actin–DNase I structures (*3*) it forms an antiparallel β turn. In the DNase I complex, in particular, the loop is attached as an additional strand to a β sheet in DNase I (*3*). Thus the DNase I binding loop, which in F-actin probably participates in intermonomer interactions (*14*), can adopt different conformations. In the ADP structure the conformational change in the DNase I binding loop, added to the ~10° rigid body rotation of subdomain 2, results in a displacement of ~14 Å for some of the amino acids at the top of subdomain 2 from their location in the ATP structures (Fig. 2). If such a structural change were to occur within F-actin, one would predict that P_i release would significantly impact the stability of the filament.

TMR is bound in the structure in a hydrophobic pocket in subdomain 1 near the profilin binding site (Fig. 1). The electron density is well defined for most parts of the probe, but the covalent bond to Cys^{374} could not be visualized because of disorder in the last three COOH-terminal amino acids. The binding of TMR changes the side-chain orientation of Tyr^{143}, Met^{355}, and Phe^{352}, which normally fill up the hydrophobic pocket now occupied by TMR. Hydrophobic stacking interactions between the TMR moieties of two actin monomers related by crystal symmetry seem to account for one of the most important crystal packing contacts in the structure.

In addition to the high-affinity site associated with the nucleotide, the high resolution of this crystal structure allowed the identification of five secondary cation-binding sites on the actin surface (occupied by Ca^{2+} in this structure). There is an extensive literature dealing with secondary cation-binding sites in actin because of their potential role in actin polymerization (*25*). Although two of the newly found sites are involved in crystal packing contacts and probably do not occur in solution, the other three are fully coordinated within a monomer and probably also exist in solution (Fig. 1).

In summary, the structural differences between ATP- and ADP-actin revealed in this work provide a model for how P_i release subsequent to ATP hydrolysis may change the conformation of the actin monomer and hence affect the dynamics of actin polymerization. In addition, the ability to crystallize monomeric actin opens the way for crystallizing actin in complex with any of the multitude of actin-binding proteins.

References and Notes

1. P. Sheterline, J. Clayton, J. C. Sparrow, *Actin* (Oxford Univ. Press, New York, ed. 4, 1998).
2. T. D. Pollard, L. Blanchoin, R. D. Mullins, *Annu. Rev. Biophys. Biomol. Struct.* **29**, 545 (2000).

3. W. Kabsch, H. G. Mannherz, D. Suck, E. F. Pai, K. C. Holmes, *Nature* **347**, 37 (1990).
4. P. J. McLaughlin, J. T. Gooch, H. G. Mannherz, A. G. Weeds, *Nature* **364**, 685 (1993).
5. R. C. Robinson *et al.*, *Science* **286**, 1939 (1999).
6. C. E. Schutt, J. C. Myslik, M. D. Rozycki, N. C. Goonesekere, U. Lindberg, *Nature* **365**, 810 (1993).
7. W. Kabsch, K. C. Holmes, *Faseb J.* **9**, 167 (1995).
8. J. H. Hurley, *Annu. Rev. Biophys. Biomol. Struct.* **25**, 137 (1996).
9. D. Pantaloni, C. Le Clainche, M.-F. Carlier, *Science* **292**, 1502 (2001).
10. C. Combeau, M.-F. Carlier, *J. Biol. Chem.* **263**, 17429 (1988).
11. P. G. Allen, L. E. Laham, M. Way, P. A. Janmey, *J. Biol. Chem.* **271**, 4665 (1996).
12. A. Orlova, E. H. Egelman, *J. Mol. Biol.* **227**, 1043 (1992).
13. L. D. Belmont, A. Orlova, D. G. Drubin, E. H. Egelman, *Proc. Natl. Acad. Sci. U.S.A.* **96**, 29 (1999).
14. K. C. Holmes, D. Popp, W. Gebhard, W. Kabsch, *Nature* **347**, 44 (1990).
15. A. Orlova, E. H. Egelman, *J. Mol. Biol.* **232**, 334 (1993).
16. S. Y. Khaitlina, J. Moraczewska, H. Strzelecka-Golaszewska, *Eur. J. Biochem.* **218**, 911 (1993).
17. A. Muhlrad, P. Cheung, B. C. Phan, C. Miller, E. Reisler, *J. Biol. Chem.* **269**, 11852 (1994).
18. Y. S. Borovikov, J. Moraczewska, M. I. Khoroshev, H. Strzelecka-Golaszewska, *Biochim. Biophys. Acta* **1478**, 138 (2000).
19. E. Kim, M. Motoki, K. Seguro, A. Muhlrad, E. Reisler, *Biophys. J.* **69**, 2024 (1995).
20. J. Moraczewska, H. Strzelecka-Golaszewska, P. D. J. Moens, C. G. dos Remedios, *Biochem. J.* **317**, 605 (1996).
21. J. Moraczewska, B. Wawro, K. Seguro, H. Strzelecka-Golaszewska, *Biophys. J.* **77**, 373 (1999).
22. Actin was prepared and labeled (*26*) at Cys^{374} with TMR from Molecular Probes. Briefly, G-actin (~6 mg/ml) in G-buffer was reacted overnight at 4°C (with stirring) with a two- to threefold molar excess of TMR, dissolved in dimethylformamide. The labeling reaction was stopped with dithiothreitol, after which the sample was exhaustively dialyzed against F-buffer (40 mM NaCl, 2 mM $MgCl_2$ added to G-buffer). Any polymerized, unreacted actin (about 5%) was removed by centrifugation at 100,000*g* for 30 min. The labeling ratio of the remaining TMR-actin was determined from the actin concentration (*26*) and the TMR concentration, which was calculated from the absorbance at the 557-nm peak with an extinction coefficient determined to be $\varepsilon = 1.06 \times 10^5\ M^{-1}\ cm^{-1}$. The labeling ratio was always between 0.9 and 1.0.
23. Crystals of TMR-labeled rabbit skeletal actin were obtained at 20°C by hanging drop vapor diffusion. In a typical experiment, 2 μl of TMR-actin (6 mg/ml) were mixed with 2 μl of a reservoir solution containing 22% polyethylene glycol 2000 monomethyl ether, 10 mM tris (pH 7.0), and 200 mM calcium acetate. A series of seeding experiments on sitting drop plates is usually required to obtain crystals suitable for diffraction. Data collection was performed at 100 K from crystals frozen in propane after addition of 13% ethylene glycol to the crystallization buffer. Two data sets were collected at IMCA-CAT beamline 17-ID and BioCARS beamline 14-BM-C at the Advanced Photon Source, Argonne, IL (Table 1). The data sets were processed with the HKL2000 package (*27*). The structure was determined by molecular replacement with the actin–DNase I structure as a search model with the program AMoRe (*28*). The model was refined to 1.54 Å resolution with the programs wARP (*29*) and Refmac from the CCP4 suite of programs (*30*). Table 1 summarizes the data collection, refinement, and model quality statistics.
24. R. Dominguez, Y. Freyzon, K. M. Trybus, C. Cohen, *Cell* **94**, 559 (1998).
25. J. E. Estes, L. A. Selden, H. J. Kinosian, L. C. Gershman, *J. Muscle Res. Cell Motil.* **13**, 272 (1992).
26. P. Graceffa *J. Biol. Chem.* **275**, 17143 (2000).
27. Z. Otwinowski, W. Minor, *Methods Enzymol.* **276**, 307 (1997).
28. J. Navaza, *Acta Crystallogr.* **A50**, 157 (1994).
29. A. Perrakis, R. Morris, V.S. Lamzin, *Nature Struct. Biol.* **6**, 458 (1999).
30. CCP4, *Acta Crystallogr.* **D50**, 760 (1994).

31. We thank H. Paulus, K. Langsetmo, and Z. Grabarek for critical reading of the manuscript. Supported by NIH grants R01 AR46524 (R.D.), P01 AR41637 (P.G.), and March of Dimes grant 5-FY99-774 (R.D.). Use of the Advanced Photon Source was supported by the U.S. Department of Energy, Basic Energy Sciences, Office of Science, under contract W-31-109-Eng-38. Use of the BioCARS facilities was supported by NIH grant RR07707. Use of the IMCA-CAT facilities was supported by the companies of the Industrial Macromolecular Crystallography Association and the Illinois Institute of Technology. Coordinates have been deposited at the Protein Data Bank (entry code 1J6Z).

8 February 2001; accepted 1 June 2001

Tauopathy in *Drosophila*: Neurodegeneration Without Neurofibrillary Tangles

Curtis W. Wittmann,[1] Matthew F. Wszolek,[1] Joshua M. Shulman,[1] Paul M. Salvaterra,[2] Jada Lewis,[3] Mike Hutton,[3] Mel B. Feany[1]*

The microtubule-binding protein tau has been implicated in the pathogenesis of Alzheimer's disease and related disorders. However, the mechanisms underlying tau-mediated neurotoxicity remain unclear. We created a genetic model of tau-related neurodegenerative disease by expressing wild-type and mutant forms of human tau in the fruit fly *Drosophila melanogaster*. Transgenic flies showed key features of the human disorders: adult onset, progressive neurodegeneration, early death, enhanced toxicity of mutant tau, accumulation of abnormal tau, and relative anatomic selectivity. However, neurodegeneration occurred without the neurofibrillary tangle formation that is seen in human disease and some rodent tauopathy models. This fly model may allow a genetic analysis of the cellular mechanisms underlying tau neurotoxicity.

Alzheimer's disease is characterized by the accumulation of abnormally phosphorylated and aggregated forms of the microtubule-binding protein tau. Aggregates of tau form intracytoplasmic neuronal inclusions known as neurofibrillary tangles. The formation of neurofibrillary tangles closely parallels the progression and anatomic distribution of neuronal loss in Alzheimer's disease (*1*), suggesting that these lesions play a role in the pathogenesis of the disorder. Mutations in the human tau gene are found in autosomal dominant neurodegenerative disorders linked to chromosome 17 (*2*). These familial disorders and similar sporadic diseases (*3*) are also characterized by extensive neurofibrillary pathology and are often termed "tauopathies." The autosomal dominant inheritance in familial tauopathies and the accumulation of abnormal tau protein in all tauopathies suggest a toxic dominant pathogenic mechanism.

To create a genetic model of these tauopathies, we expressed wild-type and mutant forms of human tau in *Drosophila melanogaster*. Wild-type tau or $Arg^{406} \rightarrow Trp$ (R406W) mutant tau, an isoform associated with an early onset, familial form of dementia, was first expressed in a panneural pattern (elav-GAL4) (*4*). The life-span of the flies was moderately shortened by wild-type tau and severely shortened by the mutant tau (Fig. 1). Western blot analysis revealed that the R406W 1 transgenic line expressed 0.8-fold less tau than the tau wild-type 1 transgenic line, indicating that the mutant tau was substantially more toxic than wild-type tau. All quantitative comparisons between wild-type and mutant tau in subsequent analyses were carried out with the tau wild-type 1 and R406W 1 transgenic lines. Tau wild-type 2 transgenic flies expressed 1.3-fold more tau than the tau wild-type 1 line. R406W 2 transgenics expressed 1.5-fold more tau than tau wild-type 1 flies. Effects of both wild-type and R406W mutant human tau on life-span were therefore dosage sensitive. Total fly brain homogenate from transgenic tau wild-type 1 animals contained about 0.5-fold less human tau protein per mg of protein than control human brain homogenate, indicating that transgenic animals did not have massive overexpression of human tau.

To determine if early death correlated with neurodegeneration, we examined the brains of tau transgenics. We first demonstrated that the nervous system of our transgenic flies was normal in newly eclosed

[1]Department of Pathology, Division of Neuropathology, Brigham and Women's Hospital and Harvard Medical School, 221 Longwood Avenue, Room 514, Boston, MA 02115, USA. [2]Division of Neurosciences, Beckman Research Institute of the City of Hope, Duarte, CA 91010, USA. [3]Mayo Clinic Jacksonville, Jacksonville, FL 32224, USA.

*To whom correspondence should be addressed: E-mail: mel_feany@hms.harvard.edu